AGU100 ADVANCING EARTH AND SPACE SCIENCE

Water Resources Research

RESEARCH ARTICLE
10.1029/2018WR022573

Key Point:
- Gas bubble storage in peat soils

Supporting Information:
- Figure S1

Correspondence to:
X. Chen,
chenxioffice@gmail.com

Citation:
Chen, X., Comas, X., Binley, A., & Slater, L. (2018). A lumped bubble capacitance model controlled by matrix structure to describe layered biogenic gas bubble storage in shallow subtropical peat. *Water Resources Research*, *54*, 5487–5503. https://doi.org/10.1029/2018WR022573

Received 10 JAN 2018
Accepted 13 MAY 2018
Accepted article online 24 MAY 2018
Published online 16 AUG 2018

A Lumped Bubble Capacitance Model Controlled by Matrix Structure to Describe Layered Biogenic Gas Bubble Storage in Shallow Subtropical Peat

Xi Chen[1,2], Xavier Comas[3], Andrew Binley[4], and Lee Slater[1]

[1]Department of Earth & Environmental Sciences, Rutgers University, Newark, NJ, USA, [2]State Key Laboratory of Earth Surface Processes and Resource Ecology, Beijing Normal University, Beijing, China, [3]Department of Geosciences, Florida Atlantic University, Davie, FL, USA, [4]Lancaster Environment Centre, Lancaster University, Lancaster, UK

Abstract Methane (CH_4) accumulates in the gaseous phase in peat soils, being released to the atmosphere at rates higher than those for diffusion and plant-mediated pathways. An understanding of the mechanisms regulating gas bubble storage in peat remains incomplete. We developed a layered capacitance model to compare the bubble storage ability of peat over different depths. A peat monolith (0.395 m $\times$ 0.243 m $\times$ 0.247 m) was collected from the U.S. Everglades and kept submerged for 102 days from a condition of minimum bubble storage to bubble saturation. Time-lapse electromagnetic wave velocity and power spectrum data were used to estimate changes in both gas content and relative average dimensions of stored bubbles with depth. Bubble capacitance, defined as the increase in volumetric gas content ($m^3\ m^{-3}$) divided by the corresponding pressure (Pa), ranges from 3.3×10^{-4} to $6.8 \times 10^{-4}\ m^3\ m^{-3}\ Pa^{-1}$, with a maximum at 5.5 cm depth Bubbles in this hotspot were larger relative to those in deeper layers, while the decomposition degree of the upper layers was generally smaller than that of the lower layers. X-ray computed tomography on peat sections identified a specific depth with a low void ratio, and likely regulating bubble storage. Our results suggest that bubble capacitance is related to (1) the difference in size between bubbles and peat pores, and (2) the void ratio. Our work suggests that changes in bubble size associated with variations in water level driven by climate change will modify bubble storage in peat soils.

1. Introduction

Following almost one decade of stable values in the 1990s, the atmospheric concentration of methane (CH_4), the second most important greenhouse gas, has increased since 2007, mandating a higher Global Warming Potential (GWP) in the most recent IPCC (Intergovernmental Panel on Climate Change) report (IPCC, 2013) relative to the previous assessment (IPCC, 2007). The IPCC notes that peatlands may contribute to the variability and uncertainty of global CH_4 emissions (Ciais et al., 2013). In peat soils, CH_4 is produced by methanogens under anaerobic conditions, and released to the atmosphere via three pathways: diffusion, transport through vascular plants and bubbling of CH_4-enriched gas, i.e., ebullition. The contribution of peat soils to the global CH_4 flux is underestimated when CH_4-enriched gas bubbles are neglected, especially as the upward transport and ebullition of CH_4-enriched gas bubbles is suggested to be the dominant pathway for CH_4 emission in peatlands (Coulthard et al., 2009; Glaser et al., 2004). A detailed description of the storage of gas bubbles needed to supply ebullition is lacking (Ebrahimi & Or, 2017; Granberg et al., 2001), in part due to the scale discrepancy between the apparent CH_4 fluxes measured over a whole peat column and the physical properties of a small peat section that control CH_4-enriched gas bubble storage. A layered model structure to describe field-scale ebullition emissions from a mudflat of an estuarine temperate marsh was recently proposed (Chen et al., 2017). In this paper, we use a general lumped capacitance model (Frank et al., 2006) as a conceptual framework to quantify the differences in bubble storage ability between layers of a peat monolith.

Two basic assumptions are considered in early computational models of bubble storage, corresponding to two stages: In stage 1, the initial CH_4 transfer from the dissolved to gaseous phase is assumed to start when the sum of the partial pressures of all gases in a gas bubble is larger than the total ambient pressure including atmospheric pressure, hydrostatic pressure, and the pressure to move soil particles (Rothfuss & Conrad,

1994; Walter et al., 1996). Assuming biogenic CH_4 is the major volatile component in peats and other wetland soils, a critical partial pressure of CH_4 can be estimated for initial bubble formation, e.g., 260 matm at 10°C, equivalent to a dissolved CH_4 concentration of 500 μM (8.0 mg L^{-1}), or a constant mixing ratio of 25% CH_4 in the bubble (Shannon et al., 1996; Walter et al., 1996). These homogenous thresholds were based on consideration of the equilibrium concentrations, i.e., the solubility of CH_4 in water, e.g., Hutchison (1957). In stage 2, given that peat and other wetland soils are very porous, most gas bubbles (~70% amount) are assumed to be released immediately to the atmosphere after formation (Walter et al., 1996; Walter & Heimann, 2000), and remaining gas bubbles are assumed to be trapped until the water table drops below the depth where they are located, or until the percentage of the pore space dominated by gas bubbles exceeds a certain critical threshold (~30%) (Walter et al., 1996).

However, continuous observations of the gas content of peat samples during controlled incubations (Baird et al., 2004; Beckwith & Baird, 2001) suggest that bubbles can grow at CH_4 concentrations below the equilibrium concentrations referenced above (e.g., 8 mg L^{-1}). Observations in organic-rich sediments, e.g., Martens & Albert (1994) also indicate that degree of supersaturation of CH_4 in near-surface pores is not high enough for direct initial formation of a bubble in a water body, i.e., homogeneous nucleation. A reasonable explanation for bubble accumulation under relatively low pore-water CH_4 concentrations is heterogeneous nucleation that starts with a gas nucleus trapped on a solid particle surface (Boudreau, 2012). Jones et al. (1999) suggest that a key requirement for heterogeneous nucleation of gas bubbles is the presence of gas cavities at solid surfaces. The nucleation energy barrier for forming a bubble in a cavity is much lower than in pore water because less interfacial free energy is needed for the bubble to grow (Boudreau, 2012). The tiny crevices, where the free gas-liquid surface needed for continuous bubble formation is maintained, are commonly termed nucleation sites.

Furthermore, CH_4-enriched gas bubbles play an important role in CH_4 storage, possibly containing more CH_4 than the pool of the dissolved phase (Fechner-Levy & Hemond, 1996). A bubble grows outward into the pore water from the solid surface until it is large enough to rise from the nucleation site, breaking away and leaving the nucleus site essentially in its original configuration (Boudreau, 2012) (Figures 1a–1c). After detachment from cavities, gas bubbles may enter the atmosphere via two processes. First, bubbles may directly rise unimpeded through pore throats from depth to the surface, resulting in regular steady ebullition (Coulthard et al., 2009) (Figures 1b and 1c). Alternatively, a released bubble may be retrapped again by a narrow pore throat, generating a new nucleation site, resulting in additional bubble nucleation sites and subsequent accumulation (Li & Yortsos, 1995b; Yortsos & Parlar, 1989) (Figures 1b and 1c). Coulthard et al. (2009) proposed reduced complexity models to simulate bubble dynamics in peat; their results show that the accumulation of bubbles look somewhat like inverted sandpiles. Results from a laboratory observation on ebullition in peat soils support this hypothesis (Ramirez et al., 2015). In fact, trapped gas bubbles in the matrix may act as a buffering reservoir, regulating changes in surrounding dissolved CH_4 concentrations (Granberg et al., 2001). The trapped gas bubbles can be released by environmental forcing or overaccumulation, termed episodic ebullition (Glaser et al., 2004).

Bubble dimension is a key parameter controlling bubble storage (DelSontro et al., 2015; Kettridge & Binley, 2008; Ramirez et al., 2016; Terry & Slater, 2017). The estimated effective radii of gas bubbles in natural peat vary widely, from less than 1×10^{-5} m (Kettridge & Binley, 2008) to 5×10^{-2} m (Terry & Slater, 2017). A minimum bubble dimension threshold for significant CH_4-enriched gas bubble storage may exist, as the gaseous CH_4 in small bubbles dissolves back to the ambient water more rapidly (DelSontro et al., 2015).

In this paper, we develop an electrical-circuit-like model from the general lumped capacitance model to explain the layered storage and charge up of CH_4-enriched gas bubbles (Stage 2 referenced above), after initial heterogeneous nucleation in a peat column (Stage 1 referenced above). This conceptual model is applied to discuss the effects of vertical variations in peat structure on bubble storage in a peat monolith. Time-lapse electromagnetic wave speed and power spectra data acquired with a ground penetrating radar (GPR) instrument are used to estimate changes in both volumetric gas content of each layer and the relative average dimensions of stored gas bubbles between depths. X-ray computed tomography (CT) on resin-impregnated peat samples from the same monolith is used to determine void ratio variations with depth. Our findings suggest that bubble capacitance of a specific peat layer is directly related to the ratio of pore throat size to gas bubble size, as well as the void ratio.

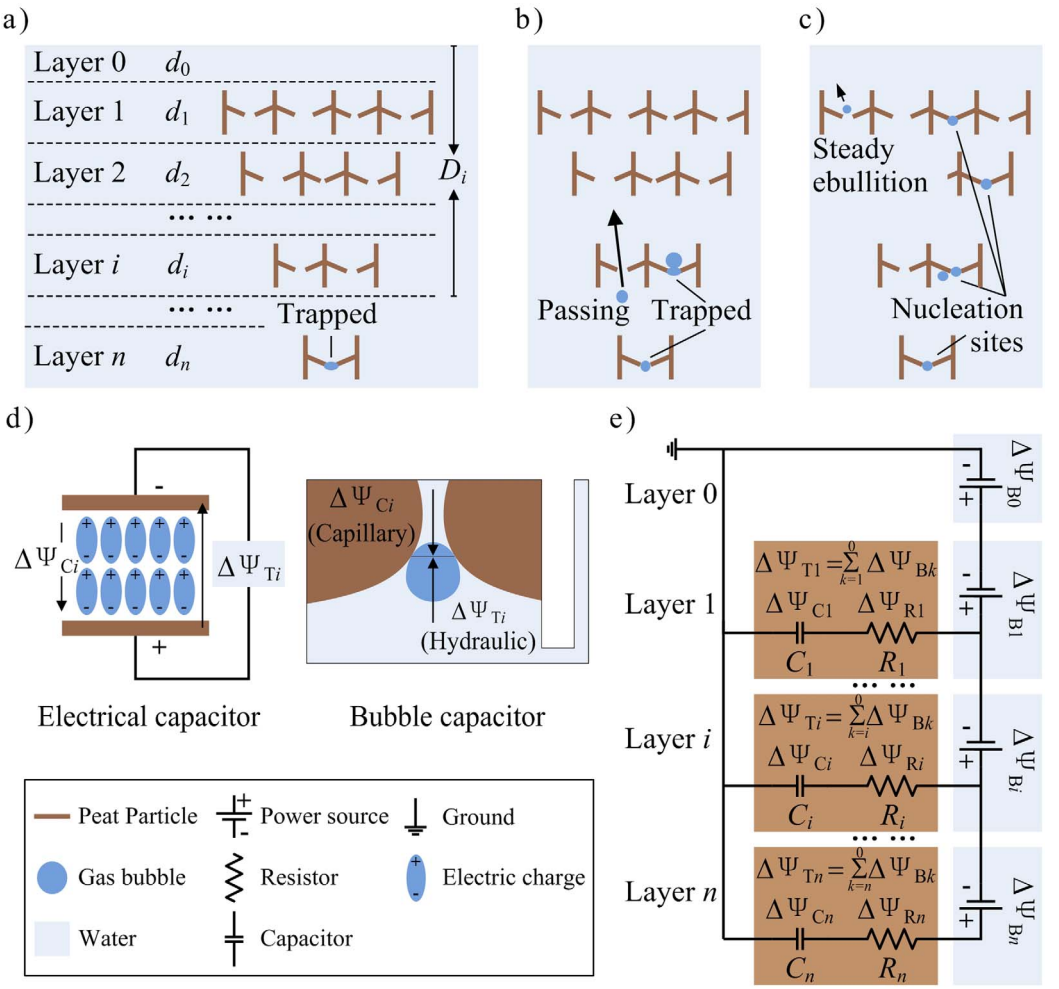

Figure 1. Conceptual model of accumulation of CH_4-enriched gas bubbles. (a–c) Heterogeneous nucleation bubble clusters move from specific nucleation sites to the upper layers (Li & Yortsos, 1995b; Yousfi et al., 1990). (d) Analogy between dielectric polarization of a capacitor and bubble entrapment in a pore throat (upward is defined as positive direction). (e) Lumped capacitance model for bubble storage. D_i, d_i, C_i, R_i, $\Delta\Psi_{Ti}$, and $\Delta\Psi_{Ci}$ represent the depth referenced to the water surface, thickness, capacitance, resistance, potential difference of the capacitor, and potential difference of energy source of the *i*th layer, respectively.

2. Lumped Capacitance Model of Gas Bubble Storage (Charge up) and Release (Discharge)

A layered model of a peat column for bubble storage and release (Figures 1a–1c) was recently proposed (Chen et al., 2017). We build on this work by defining a one-dimensional model consisting of lumped components similar to an electric circuit or a hydraulic circuit (Kirby, 2010). Entrapment (storage) of gas bubbles in pore throats is represented by the dielectric polarization of a capacitor (Figure 1d). Using this analogy, hydraulic/gravitational energy driving the bubble flux is equivalent to the total potential difference provided by a power source, $\Delta\psi_T$. Increasing the volume of entrapped gas bubbles normalized to the total volume of the layer at a depth D, i.e., the volumetric increase in gas content of the layer $\Delta\theta_g$, corresponds to increasing the total stored electric charge Q. Gas bubbles accumulate in pore throats: the average capillary potential over all the bubble entrapping pore throats at depth D increases analogous to the increase in potential difference between the two terminals of the dielectric medium of the capacitor, $\Delta\psi_C$ (Figure 1d). When a resistor is connected to the capacitor in series, the charging rate is regulated by both the resistor and capacitor. The amount of time it takes the resistor-capacitor (RC) circuit to reach a steady state condition, e.g., when the potential difference across the capacitor $\Delta\psi_C$ reaches 63% of the full-charge value $\Delta\psi_T$ (supporting information Figure S2, Hamilton, 2007), is referred to as the RC time constant τ_c of the circuit. It

Table 1
Analogous Parameters in the General Capacitance Model

	Applications		
	Electric charge storage	Soil water storage	Biogenic gas bubble storage in shallow peat
Stored property	Electrical charge	Water in soil pores	Biogenic CH_4-enriched gas bubbles
Stored amount	Stored electric charge Q	Volumetric content of pore water	Volumetric content of gas bubbles θ_g
Power source $\Delta\psi_T$	Voltage (Electric potential difference)	Hydraulic potential difference	Buoyancy
Potential difference at equilibrium $\Delta\psi_C$	Induced potential difference between the two terminals of the dielectric medium	Capillary potential against out flow of pore water	Capillary potential holding gas bubbles against buoyancy effect
Capacitance C	Electrical capacitance	(Water) Capillary capacitance	Bubble capacitance

takes a time $= 7\tau_c$ to reach 0.1% of its full-charge value $\Delta\psi_T$. This time constant τ_c depends on both the capacitance C of the capacitor and the resistance R of the coupled resistor,

$$\tau_c = \mathrm{R} \times \mathrm{C}. \quad (1)$$

Similarly, bubble resistance R in our conceptual model serves to regulate the bubble accumulation rate associated with layer dimensions (i.e., thickness for the one-dimensional model), pore structure, and fluid properties. Table 1 summarizes the analogy between components of an electrical circuit model, water capacitance model, and our bubble capacitance model.

We divide the peat column into n layers ordered from the ground surface (Layer number $i = 1$) to a certain depth D_i ($i = n$), with the surface water layer defined as Layer 0. The water level is maintained at a distance d_0 above the column surface, followed by the n peat layers of equal thickness, $d_i = d$ (Figure 1). The matrix component of each layer is represented by a capacitor (C_i) and a resistor (R_i) in series and the component that each layer contributes to the total water height is represented by a battery cell (potential energy source). The matrices of the individual layers are organized in parallel to express the capacitance of the whole peat column as the sum of the capacitances of all layers (the total gaseous volume is renormalized to the total volume of all peat layers), whereas the water heights add in series to provide linear partial potential differences corresponding to capacitor-resistor couples. The positive terminal of the ith resistor-capacitor couple is connected to the positive terminal of the corresponding ith battery cell, and all the negative terminals of the resistor-capacitor couples are connected to the negative terminal of the surface battery cell, which is grounded to a reference zero potential. With this arrangement, the potential difference between the two terminals of each resistor-capacitor couple ($\Delta\psi_{Ti}$), represents the cumulative fluid from the bottom of the ith layer to the surface of the overlying water layer, and is expressed in terms of hydraulic pressure (unit: Pa),

$$\Delta\psi_{Ti} = \rho_f g D_i, \quad (2)$$

where ρ_f is the mass density of the fluid phase, i.e., water density neglecting gas bubbles (997.05 kg m^{-3} at 25°C), g is the gravitational acceleration (9.81 m s^{-2}), and D_i is the depth from the bottom of the ith layer to the water surface,

$$D_i = \sum_{k=0}^{i} d_k, \quad (3)$$

where d_k represents the thickness of a single layer.

Our lumped capacitance model assumes that initial gas bubbles already exist and therefore focuses on Stage 2; the initial formation of CH_4-enriched gas bubbles, i.e., Stage 1, can be explained by the general concept of heterogeneous bubble nucleation from gas cavities for various solutions (Jones et al., 1999). Following initial nucleation, gas bubbles grow larger via solution transfer along concentration gradients, crossing the interface between pore water and the gas bubbles (Li & Yortsos, 1995a). The formation of a new gas bubble at an initial heterogeneous nucleation site, subsequent growth, and the later detachment from blocking pore throats is regulated by capillary pressure. The buoyancy effect resulting from gravitation has been considered the major energy source driving bubble transport across pore throats in opposition to the capillary effect (Chen & Slater, 2015; Glaser et al., 2004; Tokida et al., 2005).

In a bubble-filled cavity where the gaseous phase is in equilibrium with the dissolved phase in solution (no growth/no dissolution), the pressure difference between the two sides of the meniscus of the bubble can

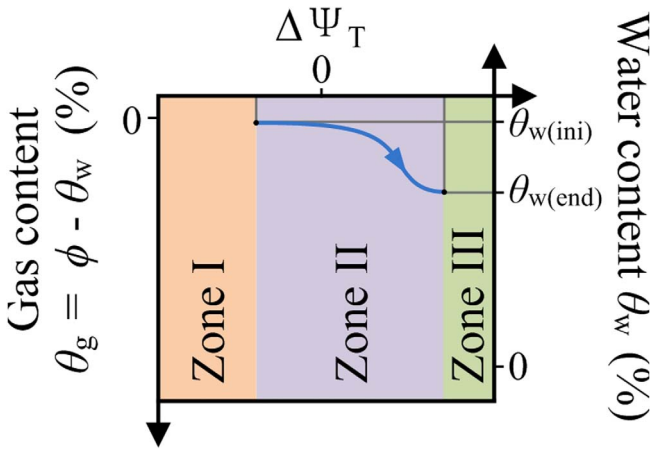

Figure 2. Zone I, II, and III represent (I) the range of regular water retention, (II) charging of biogenic bubbles, and (III) the overpressured condition with the highly uncertain possibility of breaking down the capacitor, respectively.

be described by the Laplace equation for low wetting angles (Clennell et al., 2000; Jones et al., 1999; Li & Yortsos, 1995a). Laboratory and numerical simulations suggest that bubble clusters can branch out from multiple specific nucleation sites to fill the pore network (Li & Yortsos, 1995b; Yousfi et al., 1990) (Figure 1). Therefore, concepts similar to the standard water retention curve can be used to relate volumetric gas content to capillary potential energy for a single peat layer (Figure 2). We divide the relationship between gas/water content and potential energy into three zones based on pressure ranges (Figure 2): Zone I describes regular water retention associated with trapped air bubbles and will not be discussed further; Zone II describes biogenic CH_4-enriched bubble retention of a single layer; and Zone III describes highly variable retention mainly resulting from a capacitor breakdown effect.

We first consider the bubble dynamics associated with Zone II. When the battery cells are connected to the capacitors, indicating submergence by water (Table 1), a transient direct current (DC), representing transient bubble transport, flows through the circuit to charge the capacitors, such that the potential differences across all capacitors starts increasing from zero. Once the potential difference between the terminals of the *i*th capacitor is equal to the corresponding potential difference of the power supply, $\Delta\psi_{Ti}$ (i.e., hydraulic pressure), the capacitor is fully charged and the transient current (i.e., bubble transport via a corresponding branch of the pore network) stops. Then the capacitor acts as an open circuit, i.e., $R_C = \infty$. Analogous to the definition of capillary capacity describing water storage (Richards, 1931) in Zone I, i.e., regular water retention (Figure 2), the term "bubble capacitance" C_i (unit: $m^3\ m^{-3}\ Pa^{-1}$) associated with the potential difference $\Delta\psi_{Ti}$ in Zone II describing biogenic CH_4-enriched bubble accumulation is defined as,

$$C_i = \frac{\Delta\theta_{g(i)}}{\Delta\psi_{Ti}}, \tag{4}$$

where $\Delta\theta_{g(i)}$ (unit: $m^3\ m^{-3}$) is the maximum change in volumetric gas content from the initial state $\theta_{g(ini)}$ to the final gas-saturated state $\theta_{g(sat)}$ (Figure 2). Bubble capacitance represents the total volume of gas bubbles held at pore throats in a layer under a specific hydraulic pressure, accounting for variations in bubble size and other factors. The total volume of the gas bubbles stored in the capacitors can decrease by gas bubble transport associated with episodic ebullition. Episodic ebullition events can be driven by decreases in the static hydraulic pressure on the bubbles (Chen & Slater, 2015; Glaser et al., 2004; Tokida et al., 2005), i.e., lowering the applied potential difference $\Delta\psi_{Ti}$.

We next consider the bubble dynamics occurring in Zone III. Above a particular electric field strength, the dielectric in a capacitor becomes a conductor. The voltage at which this occurs is called the breakdown voltage. However, the breakdown voltage of a material is not a precise value as there is a probability of the material failing at a given voltage. For gas bubbles in peat, once a critical potential difference $\Delta\psi_T$ similar to the breakdown voltage is applied, the *i*th peat layer no longer behaves as a capacitor but becomes a conductor. Bubble mobility after leaving nucleation sites is high as gas bubbles are relatively small, traveling freely through the interconnected pore space during stage 2 (Beckwith & Baird, 2001; Chen & Slater, 2015; Rosenberry et al., 2006). This effect may result in highly variable gas retention as observed in hydrate-controlled methane seepage from continental margin sediments (Berndt et al., 2014). Therefore, the shape of the corresponding curve is uncertain and not plotted on Figure 2.

3. Observation Methodologies

3.1. Site and Sample Collection

Laboratory observations were performed on a submerged peat monolith extracted from Water Conservation Area 3 (WCA-3) in the US Florida Everglades (Figure 3a). The site corresponds to one of the locations included in the study by Wright & Comas (2016), has a thickness of 0.72 m, and is characterized

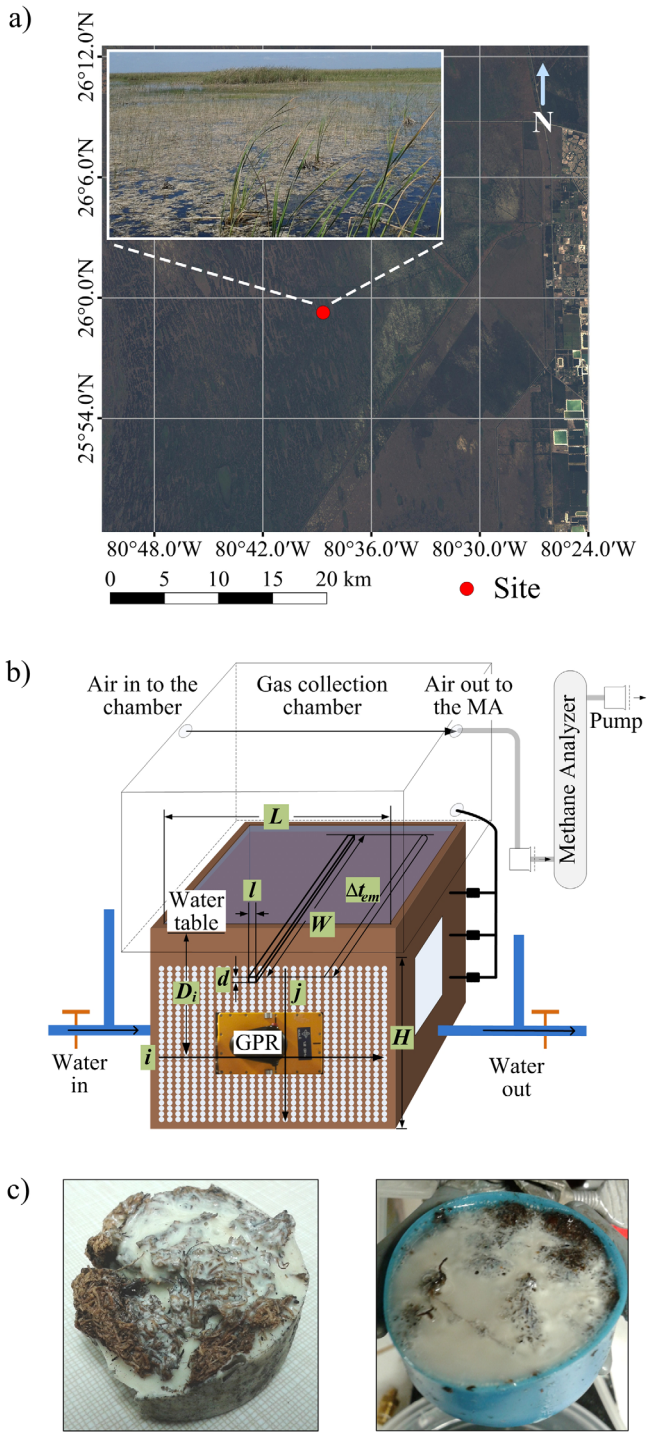

Figure 3. (a) Map showing the experimental sites; (b) Laboratory installation. *L*, *W*, and *H* are the length, width, and height of the sample, respectively; D_i is distance between the *i*th scanning line and water table; *d* and *l* are the vertical scanning interval and horizontal interval, respectively; Δtem is the two-way travel time of the electromagnetic signal through the sample monolith measured with a ground penetrating radar (GPR) device; (c) Resin-impregnated peat sections.

predominantly by Loxahatchee peat, thus dominated by water lily (*Nymphaea odorata*) plant species with a typical organic content of 92% (Craft & Richardson, 2008). The site is located in a slough, and is perennially inundated with an average water depth of 0.5 m.

A peat monolith was extracted by pushing a plastic mould box, with bottom and top removed, into the ground and then digging out the base with a saw (Comas & Slater, 2007; Parsekian et al., 2012). The monolith was cut in the laboratory (0.395 m in length *L*, 0.243 m in width *W*, and 0.247 m in height *H*, Figure 3b), transferred into a fitted sample box and equipped with noninvasive sensors and instruments similar to that described in Chen & Slater (2015).

3.2. Noninvasive Observations of Bubble Accumulation and Release

Laboratory observations, divided into three stages, were made over 102 days (5 June 2014 to 14 September 2014). Stage I involved bubble accumulation under constant conditions of water level, atmospheric pressure, and temperature to charge the "bubble capacitors" of the peat monolith (from Day 1 to Day 53). Stage II involved environmental-forcing to generate episodic ebullition events that discharge bubble capacitors (from Day 54 to Day 67). During this stage, a flow-through chamber device measured CH_4 concentration of the air in the headspace above the peat surface to determine the CH_4 concentration of the bubbles released by changing water levels. Stage III involved bubble accumulation under constant conditions of water level again to recharge those lost in Stage II, until reaching a saturated state captured in the GPR data, depending on the capacitance C_i of each layer (from Day 68 to Day 102).

3.2.1. Electromagnetic Sensing of Bubble Concentration and Average Relative Dimension

3.2.1.1. Configuration of GPR Instrument and Visual Validation

A GPR instrument equipped with a high-frequency antenna (central frequency = 1,200 MHz, MALÅ Geoscience, Sweden) was used to record the reflected electromagnetic waves from the interface between side of the container and the side of the peat monolith (Figure 3b). These signals were used to estimate variations in the total volume (Chen & Slater, 2015; Comas et al., 2007) and also to infer corresponding relative variations in average sizes of the bubbles between depths (Terry & Slater, 2017).

Two sets of measurements (details below) were made with a trade-off between temporal and spatial resolution. High spatial resolution measurements were made at 28 depths ranging from 5 to 19 cm with a vertical interval $d = 0.5$ cm ($i = 1, 2, 3, \ldots, 28$). Twenty four traces were recorded at each depth between 8 and 32 cm from the left side of the monolith with a horizontal interval $l = 1$ cm ($j = 1, 2, 3, \ldots, 24$). The scanned area (0.140 m × 0.240 m) was smaller than that of the actual monolith side (0.243 m × 0.395 m) to account for the footprint of the GPR antenna. Four such scans were collected in Stage I (Day 2, Day 18, Day 40, and Day 53) with an additional three scans collected in Stage III (Day 68, Day 89, and Day 102), allowing six time-difference images to be created. Collected signals at all the sampling points (*i*, *j*) were used to estimate the changes in volumetric gas contents and then the layered bubble capacitances (section 3.2.1.2). Four locations P1 ($i = 5, j = 2$), P2 ($i = 5, j = 14$), P3 ($i = 26, j = 2$), and P4 ($i = 26, j = 14$) were

analyzed to compare relative bubble dimension between depths (Terry & Slater, 2017) from the seven time slices using Matlab (Mathworks, Inc. 2012) (section 3.2.1.3).

Low spatial resolution measurements at four depths of 5 cm (i.e., layer $i = 1$), 8.5 cm ($i = 8$), 12 cm ($i = 15$), and 18.5 cm ($i = 28$) with a horizontal interval of 2 cm were made during Stage I only. Two measurements per day (one between 9:00 and 10:00 and another between 17:00 and 18:00) were collected from Day 1 to Day 46 to confirm continuous bubble accumulation with a fine temporal sampling interval. Direct observations of bubble accumulation were also made by visual counting of gas bubbles appearing on the transparent edge of the box during Stage I only. Bubble counts as a function of depth were qualitatively estimated by tracing macroscopic bubbles appearing on the side of the tank, with tracings digitized for subsequent analysis (Chen & Slater, 2015; Liu et al., 2016; Ramirez et al., 2015).

3.2.1.2. Bubble Capacitance Estimation From Changes in Gas Content

To estimate the bubble capacitance C_i (equation (4)) of the ith layer, the total volumetric content of accumulated gas bubbles $\Delta\theta_{g(i)}$ was calculated from the difference between the initial volumetric gas content $\theta_{g(i,j,ini)}$ and the final bubble-saturating gas content $\theta_{g(i,j,end)}$,

$$\Delta\theta_{g(i)} = \sum_{j=1}^{24} \left(\theta_{g(i,j,end)} - \theta_{g(i,j,ini)}\right), \tag{5}$$

where the index i indicates different depths of the monolith beginning from the top line of GPR scanning, index j indicates different subcolumns referenced to the left edge of the GPR scanning and t indicates date of the observation. We assume minimum gas storage, i.e., the peat column is close to 100% water saturation at the start of the experiment. The bubble capacitances C_i (i, j) [$i = 1, 2, 3, \ldots, 28$; $j = 1, 2, 3, \ldots, 24$] cover a part of the strips of the entire volume (i', j') [$i' = 11, 12, 13, \ldots, 38$; $j' = 9, 10, 11, \ldots, 32$] due to the footprint of the GPR antenna. Gas content $\theta_{g(i,j,t)}$ is regarded as the difference between total porosity $\phi_{(i,j,t)}$ and water content $\theta_{w(i,j,t)}$,

$$\theta_{g(i,j,t)} = \phi_{(i,j,t)} - \theta_{w(i,j,t)}. \tag{6}$$

Bulk dielectric permittivity ε_b of the peat monolith depends on the dielectric permittivity and volume concentration of the three phases (solid, gas and liquid). The bulk relative permittivity ε_b was estimated by correcting the two-way travel time Δtem of the electromagnetic signal through the sample monolith. Assuming low dielectric loss,

$$\varepsilon_b = \left(\frac{\upsilon \Delta \mathrm{tem}}{2W}\right)^2, \tag{7}$$

where υ is the speed of the electromagnetic wave in free space and W is the distance between the GPR antenna and reflection interface, i.e., 24.3 cm (Figure 3b). Previous work directly links the gas content θ_g to the bulk dielectric permittivity ε_b, e.g., with the Complex Refraction Index Model (CRIM) (Comas et al., 2005, 2011). However, this requires a reliable estimate of $\phi_{(i,j,t)}$, which proved impractical in this study. Water content θ_w can instead be estimated from the bulk relative permittivity with an empirical third-order polynomial, e.g., the Topp model for mineral soils (Topp et al., 1980), avoiding the need for a porosity estimate. A specific polynomial function with calibrated coefficients for *Sphagnum* peat at high saturation conditions (Kellner & Lundin, 2001) was directly applied to the sawgrass peat monolith with tolerable structure bias,

$$\theta_w = 3.9\times10^{-2} + 3.17\times10^{-2}\varepsilon_b - 4.5\times10^{-4}\varepsilon_b{}^2 + 2.6\times10^{-6}\varepsilon_b{}^3 \ . \tag{8}$$

Substituting equation (7) into (8), the water contents in different saturation states $\theta_{w(i,j,t)}$ can be estimated.

It was not possible to acquire porosity measurements on every individual cell [i, j] within the monolith using a gravimetric method. The differential form of equation (6) states that the increase in volumetric gas content of each cell approximates the decrease in volumetric water content,

$$\theta_{g(i,j,end)} - \theta_{g(i,j,ini)} = \theta_{w(i,j,ini)} - \theta_{w(i,j,end)} + \Delta\phi_{(i,j)}, \tag{9}$$

where $\Delta\phi_{(i,j)}$ is an additional correction term for pore expansion during bubble accumulation (Chen & Slater, 2015). Here, this correction is assumed to be negligible as the gas contents were lower than the saturation values associated with significant pore expansion. Therefore, bubble capacitance (C_i) can be

calculated from water content estimates ($\theta_{w(i,j,t)}$) determined from dielectric permittivity measurements with matrix expansion ignored. Substituting equation (9) into (5), the total increase in volumetric gas content is,

$$\Delta\theta_{g(i)} = \sum_{j=1}^{24} \left(\theta_{w(i,j,ini)} - \theta_{w(i,j,end)}\right), \tag{10}$$

where the absolute water contents $\theta_{l(i,j,ini)}$ and $\theta_{w(i,j,end)}$ at the start of Stage I and the end of Stage III, respectively, were determined from GPR measurements. Substituting equations (2), (3), and (10) into (4), the layer-averaged bubble capacitance C_i of the ith layer is,

$$C_i = \frac{\sum_{j=1}^{24} \left(\theta_{w(i,j,ini)} - \theta_{w(i,j,end)}\right)}{\rho_f g \sum_{k=0}^{i} d_k}, \tag{11}$$

where the initial water level relative to the peat monolith surface, d_0, is 5.7 cm.

The same approach was used to estimate changes in bulk relative permittivity ε_b during the period of higher temporal resolution (twice per day within Stage I). GPR measurements were acquired at low spatial resolution (four depths with a horizontal interval of 2 cm). These measurements confirmed the temporal continuity of gas accumulation due to steady biogenic CH_4 production over a long time period.

3.2.1.3. Changes in Average Bubble Dimensions

To obtain some insight into the changes in average bubble dimension during bubble accumulation, the power spectrum of the received GPR signal was calculated following the approach outlined by Cassidy (2008) and Terry & Slater (2017). Comas et al. (2005) suggest that clusters of gas bubbles in peat may result in obvious scattering attenuation in GPR signals. The scattering response is related to signal frequency, or alternatively the corresponding wavelength of the electromagnetic signal relative to average bubble size (Terry & Slater, 2017). Small gas bubbles result in highly frequency-dependent Rayleigh scattering, i.e., less signal attenuation at low frequencies relative to higher frequencies. As gas bubbles grow larger, the scattering response becomes more uniform Mie scattering, whereby different frequencies exhibit similar decay characteristics (Terry & Slater, 2017).

The total attenuation in the EM signal passing through a multiphase material includes both scattering and absorption components. Forward simulations for reference signals, prior knowledge, and appropriate assumptions are necessary to solve the inverse scattering problem, e.g., estimating change in the average dimension of gas bubbles (Terry & Slater, 2017), or the distribution pattern of light nonaqueous-phase liquids (LNAPLs) (Cassidy, 2008). Simulation results using the finite-difference time-domain (FDTD) method show that, in the Rayleigh scattering range, peak frequency shifts toward lower frequencies with increases in the volumetric content of the scattering objects when they meet specific geometrical and spatial distribution conditions (Cassidy, 2008). Terry & Slater (2017) argued that relative changes in the frequency power spectra are mostly sensitive to the changes in size of bubbles accumulating in peat, i.e., bubble size dominates the frequency spectra for peat soils. As gas content increases with increasing bubble size, small frequency shifts in the low-frequency Rayleigh scattering region indicate the dominance of Mie scattering due to the accumulation of relatively large bubbles, as assumed to occur here.

3.2.2. Flow-through Chamber Method for CH_4-Enriched Bubble Release

Controlled pore pressure changes were achieved by slow inflow of water to increase the pressure head above the initial saturated condition, and slow outflow to decrease the pressure head until the initial saturated condition was again achieved (Figure 3b). Raising and lowering the water table of the bottom chamber was performed at a controlled slow rate once daily (Figure 3b).

The CH_4 flux in the upper chamber above the sample monolith was monitored using a methane analyzer (MA) sealed in a matched calibration shroud (LI-7700, LI-COR Inc.). At the 1 Hz sampling rate of the methane analyzer (f_{MA}=1 Hz), a pump transported $2.8 \pm 0.1 \times 10^{-4}$ m^3 of CH_4 containing carrier gas between each time slice (1 s). The absolute pore-pressures were measured with three vented pressure transducers (26PC Series, Honeywell Sensing and Control) installed 4.5, 11.5, and 18.5 cm below the water table (Figure 3b).

3.3. Peat Humification and X-Ray CT Scanning

At the end of the experiment, the peat sample was destructively extracted layer-by-layer to determine the vertical variations in structure from humification estimates and X-ray CT scanning measurements. Degree of

humification was estimated for five layers between 0 and 24.7 cm depth. Samples from each layer were squeezed by hand to determine the texture and color of peat, and the color of drained water. The von Post standard (von Post, 1922) was used to quantify relative decomposition.

Blais (2005) and Kettridge and Binley (2008) demonstrated that it is possible to extract information on pore size and pore continuity from X-ray images. In this research, X-ray computed tomography (CT) scanning was used to measure the corresponding vertical distribution of void ratio hypothesized to control bubble storage. A peat column (height = 24.7 cm, diameter = 4.4 cm) was extracted from the peat monolith with a PVC cylinder with minimum compression, and cut into 18 slices each of height 1.4 cm. To retain the peat structure, each slice was cast by dehydration with acetone and impregnated with low viscosity resin (Alumilite, Kalamazoo, MI; Figure 3c) (Quinton et al., 2008). All peat samples were scanned around the center of rotation with an X-tek Benchtop CT160Xi CT scanner (X-Tek Systems Ltd, UK) and a dual field image intensifier coupled to a digital charged couple device (CCD)) (Kettridge & Binley, 2008, 2011) at 5 micron resolution. The 360 × 360 pixels forming the middle region of the central 50 radiographs of each peat section were stacked and used for statistical analysis.

The histograms of voxel intensities recorded on the peat samples are assumed to represent the combination of two normal distributions (Rezanezhad et al., 2009), corresponding to the peat matrix particles and resin, i.e., pores, respectively. The voxel intensities of all slices of each section were fit with the Expectation-Maximization algorithm for mixtures of univariate normals using RStudio (Version 1.0.136, RStudio, Inc. Boston, MA). To account for variations in CT signal decay between different sections, the voxel number ratios r1 and r2 representing the number of voxels in the resin intensity range and the number of voxels within the peat particle intensity range to the total number of all voxels respectively, were calculated (r1 + r2 = 1). The r1 values indicate relative variations in void ratio between depths, which can be compared with the vertical distribution of bubble capacitances C_i.

4. Results

Time-lapse dielectric permittivity measurements provided a 2-D image of the accumulation of gas bubbles within the monolith, allowing the computation of bubble capacitances representing the maximum bubble storage ability at different depths. The power spectra of the GPR data provide information on changes in relative bubble dimensions between layers. The flow-through chamber system confirmed that these gas bubbles were CH_4-enriched, whereas destructive analysis including von Post numbers and X-ray CT measurements identified distinct variations in physical properties of peat with depth in the peat block related to the variations in bubble storage. Specific results relating to each measurement are provided below.

4.1. Changes in Gas Content and Bubble Capacitance

Based on the bulk relative permittivity results at high spatial resolution (Figures 4a–4g), the water contents at all 28 measurement depths generally decreased across Stages I and III (Figures 4h–4k, and 4l–4n). The time-difference images suggest that gas contents at all 28 measurement depths increased across Stages I and III as a result of bubble accumulation (Figures 4o–4q, and Figures 4r–4t), and decreased by bubble release, i.e., ebullition driven by environmental forcing, during Stage II (Figures 4q–4r). These increases in gas content were greatest at 5–10 cm depth (Figure 5a), gradually reaching the maximum gas contents at the end of Stage III (Figure 5b). However, at some locations in this hotspot layer, e.g., point P1 ($i = 5, j = 2$), the maximum change in gas content $\Delta\theta_{g(5,2)}$ was only 0.57% (Figures 4o–4t), suggesting that this region remained water-saturated with little gas bubble accumulation over time. The final bubble capacitances C_i (equation (11)) of all layers ranged from 3.3×10^{-4} to 6.8×10^{-4} $m^3\ m^{-3}\ Pa^{-1}$, with the maximum value located at 5.5 cm depth (Figure 5c).

Based on the bulk relative permittivity results at high temporal resolution (Figure 6a), gas bubbles continuously accumulated at four depths; occasional increases in the bulk relative permittivity highlight decreases in gas content resulting from minor ebullition events. Hand-drawing of gas bubbles observed on the chamber side provided a direct estimation of bubble accumulation (Figure 6b). The areal percentage of macroscopic bubbles in every layer i increased over the initial state. Consistent with the dielectric permittivity results, the largest areal percentage of macroscopic bubbles during the entire measurement period was observed in the 5–10 cm depth layer.

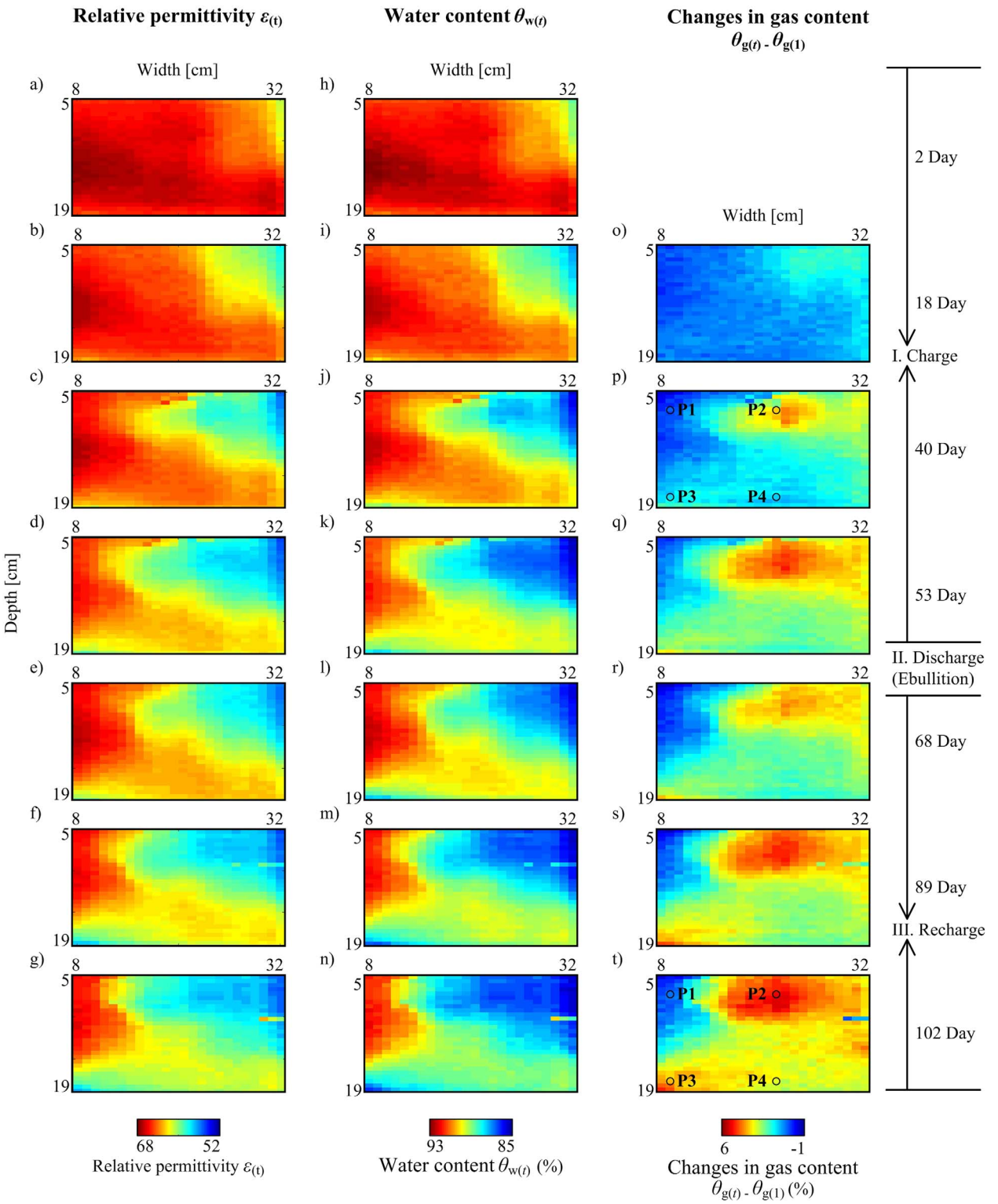

Figure 4. Relative permittivity, estimated water content, and changes in gas contents with GPR scanning on Day 2, 18, 40, 53, 68, 89, 102 during Stage I and III of the observation period. The changes in water contents between the initial state and end state were used to estimate gas contents, and thereby gas capacitance.

4.2. Changes in Relative Average Bubble Dimension

Four locations P1 ($i = 5$, $j = 2$), P2 ($i = 5$, $j = 14$), P3 ($i = 26$, $j = 2$), and P4 ($i = 26$, $j = 14$) were selected (Figure 4t) for GPR power spectrum analysis to estimate relative changes in bubble dimension between

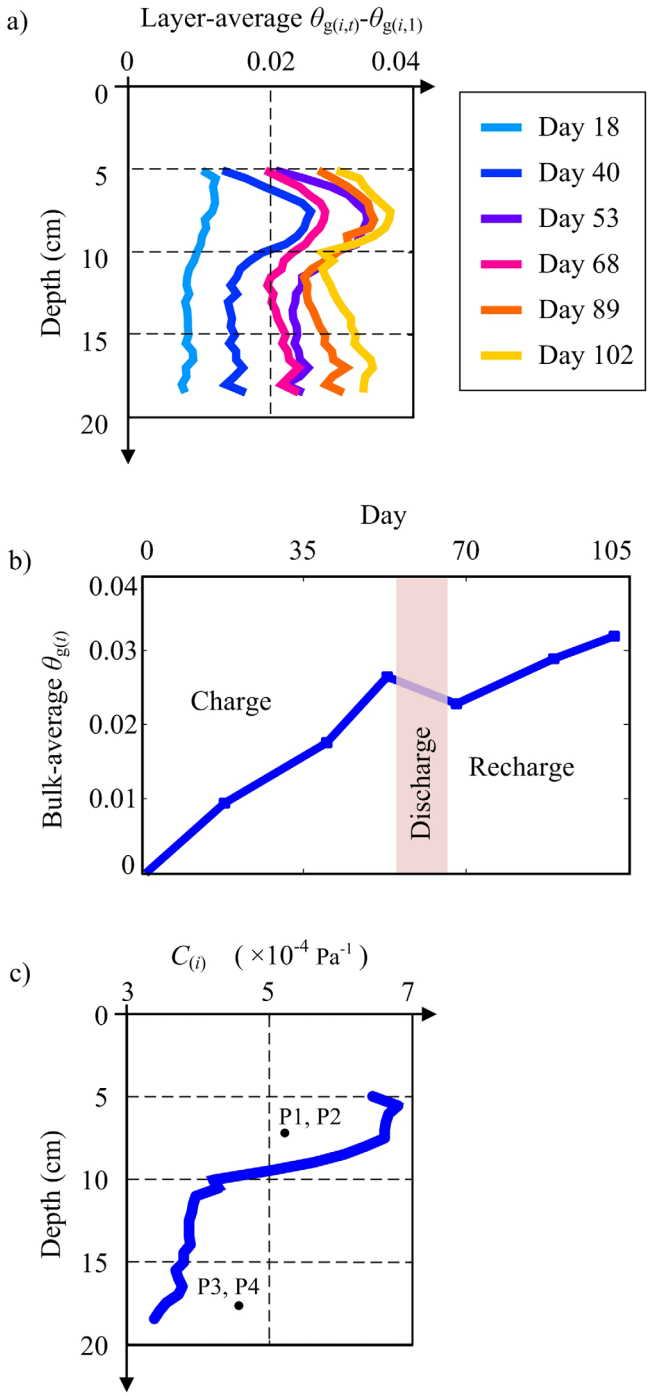

Figure 5. Result of changes in gas content. (a) Layer-averaged increases in gas contents on Day 18, 40, 53, 68, 89, 102 during the observation period. (b) Bulk averaged gas contents during the observation period. (c) Bubble capacitances of each depth.

layers during bubble accumulation (P2 and P3 in Figure 7, P1 and P4 in supporting information Figure S1). Gas contents at point P2 showed the largest increases among these four points (Figures 4o–4t); the high-frequency peaks in the spectra (Figure 7a) are consistent with the dominance of Mie scattering attenuation (Terry & Slater, 2017), suggesting accumulation of large gas bubbles. Points P1 and P4 are characterized by little continuous change in the spectra (supporting information Figure S1a and S1b), associated with small changes in gas contents during Stages I and III (Figures 4o–4t). The small frequency shift at P1 between Day 18 and Day 40 (supporting information Figure S1a) is consistent with steady ebullition events, along with a few large bubbles being released into the atmosphere such that the corresponding pore space was invaded by small gas bubbles from deeper layers. Point P3 showed continuous decreases in the amplitudes of the spectra over time (Figure 7b). According to the simulated attenuation patterns (Terry & Slater, 2017), the relatively greater attenuation at the high frequencies over time indicates the dominance of Rayleigh scattering attenuation, which can be ascribed to the increases in the number and/or size of gas bubbles. Attenuation due to absorption should be reduced in the presence of gas bubbles because of the high resistivity of the bubbles (Terry & Slater, 2017).

4.3. Ebullition During Forced Changes in Hydrostatic Pressure

Changes in the CH_4 concentrations recorded during the periods of forced hydrostatic pressure changes are summarized in Table 2. Decreases in average pressure heads ranged from 2.0 to 10.4 cm, with an average value of 4.08 cm. Corresponding increases in the CH_4 concentration in the upper chamber Δc ranged from 88.4 to 505.0 mmol m^{-3}, with an average value of 252.76 mmol m^{-3}, proving that the released gas bubbles are CH_4-enriched relative to the atmospheric concentration.

4.4. Peat Humification and X-Ray CT Scanning

The von Post scores for humification degree at five depth intervals (Table 3) indicate that the upper peat (depth 0–10 cm) was less decomposed than the lower peat (depth 10–25 cm). The shallow peat of the upper layer (depth 5–10 cm) showed variations in humification degree between H2 to H3, containing a peat fabric, e.g., consisting of undecomposed coarse roots of vascular plants, that retained its overall shape after oven drying (Figure 8a). The lower peat below a depth of 10 cm exhibited a gradual increase in decomposition degree per the von Post score H3 to H5 toward the bottom (Figure 8a). The void ratios r1, i.e., the number of voxels in the resin intensity range relative to the total number of all voxels of the CT scanning images (Figure 8a) exhibit two minima (0.06 and 0.18 at depths of 4.9 and 18.9 cm, respectively), indicating low void ratios relative to other depths in the monolith. The smallest r1 value at 4.9 cm depth is located just above a peak value of bubble capacitance C at 5.5 cm depth (Figure 5c), suggesting a barrier structure limiting vertical movement of bubbles. This suggests that the peat fabric between 5 and 10 cm depth partly regulates gas accumulation (Chen & Slater, 2015; Comas et al., 2011; Glaser et al., 2004; Rosenberry et al., 2003). The r1 values below 16.1 cm depth are overall smaller than the values for the upper layers between 9.1 and 14.7 cm depth, indicating a decrease in void ratio.

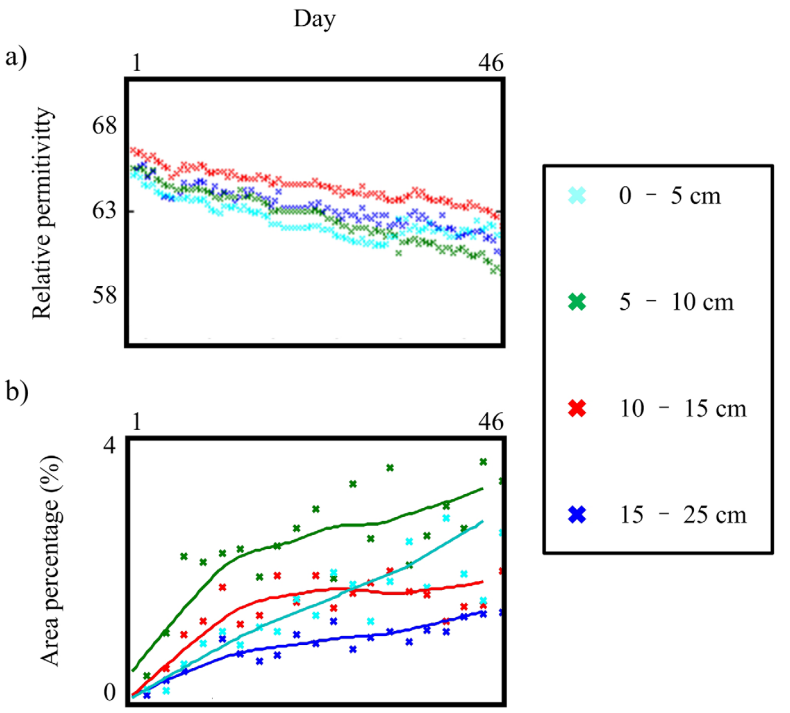

Figure 6. Results of estimated long-term changes in gas content at four depths: (a) Time-lapse layer-averaged relative permittivity based on GPR measurement. The value of each layer represents the average of 12 traces at corresponding depth and (b) area percentage of gas bubbles hand-drawn from scanning images.

5. Discussion

The general capacitance model provides a convenient way to physically link peat physical properties to bubble storage and release, leading to new understanding of the controls on bubble storage. We conducted laboratory observations on a subtropical peat monolith for estimating bubble capacitances at different depths and discussing the roles of peat structure. Gas dynamics were inferred from time-lapse changes in volumetric gas content and relative average bubble size estimated from electromagnetic wave velocity and power spectra acquired with the GPR instrument, coupled to CH_4 concentrations of released gas bubbles from the peat sample acquired using a flow-through chamber system. Destructive analysis based on humification estimates combined with X-ray CT scanning identified distinct variations in the physical properties of peat between different depths that seem to dictate changes in gas content and average bubble dimensions. The vertical distribution of computed bubble capacitances *C* that represent the maximum bubble storage capability of the peat revealed a hotspot layer of bubble storage at 5.5 cm depth, below a barrier zone limiting vertical movement of bubbles.

5.1. Initial Source of Heterogeneous Nucleation Sites for Bubble Formation

Our physical model mainly focuses on bubble accumulation (Stage 2) after initial bubble nucleation (Stage 1). Three possibilities are suggested for the initiation of heterogeneous nucleation sites: Firstly, we assume that microbubbles form readily and act as seeds for later growth (Baird et al., 2004; Coulthard et al., 2009). These preexisting seeds can be ascribed to pockets of air bubbles trapped in shallow peat during water-table rise (Baird et al., 2004; Beckwith & Baird, 2001; Coulthard et al., 2009), that grow bigger via inward diffusion of biogenic CH_4. Second, a nucleus may form in a small pore pocket under conditions of supersaturation, although the measured dissolved CH_4 concentration will only represent an "average" value for a much larger volume with mostly low CH_4 concentration. Furthermore, the CH_4 concentration in gas bubbles can vary substantially, e.g., between 9% and 77% over time (Mustasaar & Comas, 2017), suggesting significant heterogeneity in dissolved CH_4 concentration in pore water and frequent mass exchange between the gaseous phase and dissolved phase. Spatiotemporal variations in both dissolved and gaseous CH_4 concentration observed by Mustasaar and Comas (2017) were ascribed to changes in CH_4 production

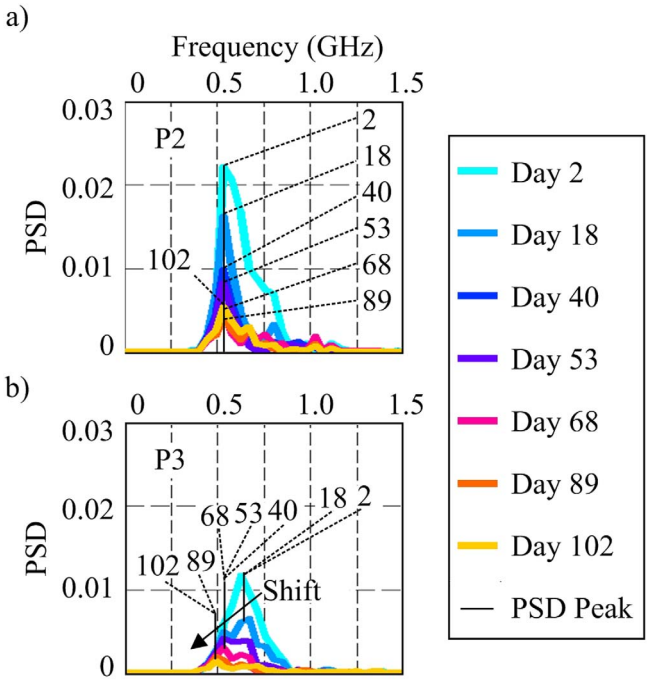

Figure 7. Power spectra associated with GPR scanning at sampling points P2 and P3. P3 exhibits frequency shifts over the whole period whilst P2 shows a more constant attenuation pattern, suggesting that scattering responses at P2 and P3 are Mie and Rayleigh type, respectively.

within the peat sample, probably in relation to changes in plant composition and/or quality of organic matter content making up the hotspot area. Third, Boudreau (2012) suggested that, as much sedimentary material is formed subaerially in terrestrial environments, trapping of gas during its formation is likely common. Such gas bubbles retained in the sediments below the peat may enter the overlying peat and become trapped again, acting as heterogeneous nucleation sites.

5.2. Effects of Peat Void Ratio on Bubble Capacitance

Volumetric gas content estimates from dielectric permittivity measurements indicate a hotspot of gas bubble accumulation in the upper layer (e.g., 5.5 cm depth with the peak value of bubble capacitance *C*), as bubbles are not necessarily released immediately upon formation (Beckwith & Baird, 2001; Rosenberry et al., 2003). Kettridge & Binley (2008) used X-ray computed tomography (CT) to describe the distribution of individual gas bubbles within *Sphagnum* peat and corresponding peat structures in the laboratory, and found that most gas bubbles (ranging from 0.1 to 99.9 mm^3) clustered near the surface of a peat sample extracted from ground surface to a depth of 13 cm, being consistent with our GPR-based observations on Loxahatchee peat (Point 2 in Figure 4t).

Variations in peat stratigraphy have previously been suggested to regulate bubble storage in specific layers within different soil columns, and control the redistribution of gas bubbles (Chen & Slater, 2015; Kettridge & Binley, 2008; Wright & Comas, 2016). The smallest void ratio r1 at 4.9 cm depth suggests the presence of a barrier structure in the surface layer, being ascribed to the decay of poorly decomposed roots and stems of vascular plants (Figure 8). This barrier structure is located above the peak value of bubble capacitance *C* found at 5.5 cm depth (Figure 5c). Variations in the von Post humification metric (Figure 8a) suggest a predominantly two-layer model: the upper layer (e.g., depth 0–10 cm) is less decomposed (Quinton et al., 2008). Poorly decomposed materials can form a barrier structure supporting bubble storage immediately below. The lower layer of small r1 values is associated with more decomposed peat, causing a decrease in the size of particles and interparticle pores with depth, and an increase in the amount of solid material per unit volume (Quinton et al., 2000).

5.3. Effects of Average Bubble Dimension on Bubble Capacitance

Based on the changes in the spectra of the EM waves transmitted through peat (Terry & Slater, 2017), the relative average bubble radii (Figure 7 and supporting information Figure S1) at different depths can be estimated and compared with the vertical distribution of bubble capacitances *C*. Although the absorption attenuation of simulated EM signals due to electrical conductivity is larger than that due to scattering across all frequencies investigated, the shape of the power spectra reflects both absorption and scattering contributions, and is particularly sensitive to changes in the size of bubbles accumulating in peat, i.e., bubble size dominates the frequency spectra for peat soils (Terry & Slater, 2017).

This comparison suggests that more large bubbles accumulate in the upper layer (e.g., Point P2 in Figure 7a) relative to the bottom layer (Point P3 in Figure 7b). Hydroacoustic observations of gas bubbles released from organic-rich lake sediments into the upper water column indicate that ebullition events are mostly composed of large bubbles, e.g., diameter > 14 mm in Kiel harbor, Germany (Greinert & Nützel, 2004) or diameter > 10 mm in Lake Wohlen, Switzerland (Del-Sontro et al., 2015). We assume that large gas bubbles are stored in the upper layer, resulting in the high value of bubble capacitance *C* at

Table 2
Decreases in Hydrostatic Pressure (Average = 4.1 cm, Standard Error = 3.6 cm) and Corresponding Increases in CH_4 Concentrations (Average = 252.8 mmol m^{-3}, Standard Error = 180.1 mmol m^{-3}) During Stage II

Events	Average decreases in hydrostatic pressure (cm)	Increases in CH_4 concentration (mmol m^{-3})
1	2.0	213.6
2	3.3	363.3
3	2.6	93.5
4	10.4	505.0
5	2.1	88.4
Average	4.1	252.8
Standard error	3.6	180.1

Table 3
Structural Parameters of Each Layer

Layer i	Depth (cm)	von Post humification
1	0–5	H2 – H3
2	5–10	H2
3	10–15	H3
4	15–20	H4
5	20–25	H5

the depth of 5.5 cm (Figure 5), with release of these bubbles into the water body above (Layer 0 in Figure 1).

A larger volume of a single bubble in the upper layer is consistent with gas bubble expansion due to lower pore pressures in the underlying layers; Differences in the pore-size distribution of the peat sample will lead to differences in the ability of the peat to trap and subsequently release bubbles (Baird et al., 2004). Three-dimensional (3-D) analysis of peat pore structure from previous X-ray CT scanning on peat soils also suggests that the pore network is dominated by a single large pore-size (Rezanezhad et al., 2009). Therefore, only correspondingly larger gas bubbles can be held by these pore throats in the upper layer, as bubbles otherwise directly pass by. Finally, larger bubbles may rise faster than smaller bubbles (Corapcioglu et al., 2004), and thus are more likely to bypass consumption by methanotrophs (Ramirez et al., 2016).

5.4. Limitations and Extension

The 1-D layered model structure represents a significant simplification. Indeed, spatial heterogeneity in bubble storage exists in the horizontal plane as confirmed by the GPR data (e.g., Points 1 and 2 in Figure 4t). Direct visual observation via the clear chamber wall qualitatively supports the vertical variation in gas contents over different depths, but the absolute accuracy is limited because of the wall effect on bubble storage (Chen & Slater, 2015; Liu et al., 2016). The bubble capacitance defined in this paper is focused on the

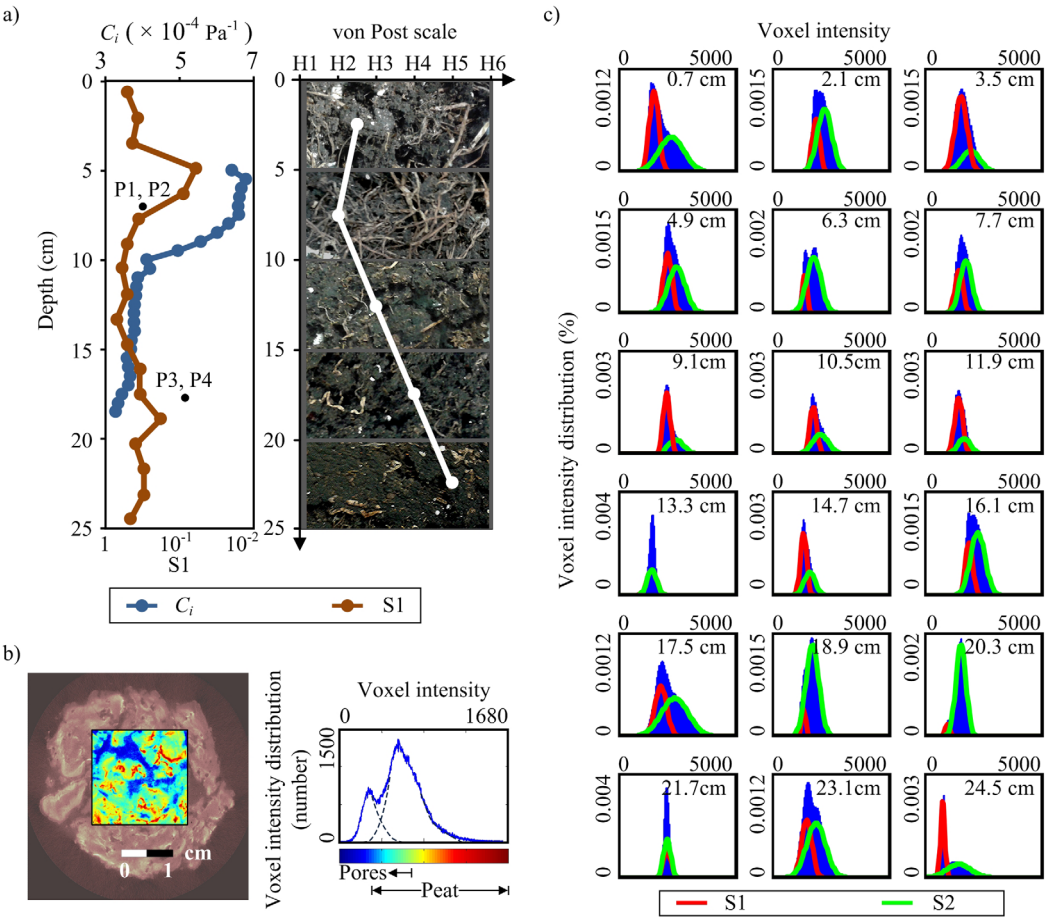

Figure 8. Vertical variation in peat structure: (a) values of void ratio r1, bubble capacitance C_i, von Post humification and corresponding photos at different depths. (b) A sample slice of X-ray CT scanning of peat section and the corresponding histogram of voxel intensity; (c) Histograms of voxel intensity of 18 sections of the peat sample showing the volume contrast between resin-filled pore space (r1) and peat particles (r2).

volumetric content of stored gas bubbles. However, CH_4 concentration in gas bubbles was recently found to vary substantially (Mustasaar & Comas, 2017).

The form of water deserves consideration when applying equation (8) to estimate the volumetric water content for the change in gas content from the bulk relative permittivity of each peat layer. The gas content estimates from equation (8) may be affected by bound water on peat particle surfaces, depending in part on the decomposition degree of the layer (Kellner & Lundin, 2001; Yu et al., 1999). In practice, estimates of bound water needed to improve calibration functions are difficult to obtain, and may not significantly improve the estimation of volumetric water content in pores (Kellner & Lundin, 2001). Structural water that constitutes part of the organic matter lattice has little effect on bulk dielectric properties, compared with that of pore-filling water (Marfunin, 1994).

Furthermore, the rigidity of the peat skeleton regulates deformation of the pore space. Gas bubbles can enlarge the pore space when the exerted pressure is high enough (Chen & Slater, 2015). Changes in porosity were considered in this paper but were not estimated for each small cell making up the 2-D plane due to lack of measurements with sufficient accuracy. In addition, the preparation of the peat samples for CT scanning, involving slicing the peat to remove moisture with acetone followed by impregnating the peat with resin (Quinton et al., 2008), may have caused some shrinkage of the pore network. Alternatively, the peat may secrete wax, making it difficult to image the pore structure (Quinton et al., 2009) and accurately estimate void ratios. Finally, gas bubbles in peat can not only accumulate behind existing bubbles lodged in pore necks (Baird & Waldron, 2003; Kellner et al., 2006; Strack et al., 2005), as considered in this paper, but also underneath woody layers, or below well-decomposed layers of peat (Glaser et al., 2004; Rosenberry et al., 2003). Under the latter condition, fracture mechanisms similar to those occurring in fine-grained sediments are possible (Jain & Juanes, 2009).

Our conceptual model is general and applicable to most two-phase fluid problems in a porous matrix, e.g., other soil types and gas components, extending the system state analysis with a lumped element model. The concept of "bubble capacitance" links the gas content to environmental pressures with special water retention curves (Figure 2), suggesting additional controls on bubble storage and release beyond the ideal gas law. Using this concept can improve interpretation of observations of gas bubble formation, accumulation, and interaction with matrix structure. Changes in gas content might be estimated from the model if discharging and charging of a bubble capacitor are assumed reversible. However, the hysteresis phenomenon commonly observed in soil moisture retention would have to be considered. The time constant τ_c of the model only represents the maximum time required to release a specific volume of gas bubbles associated with decreases in water level, i.e., the occurrence of individual episodic ebullition events cannot be accurately predicted with the model.

6. Conclusions

Bubble capacitance developed from a general capacitance model provides new understanding of the effects of capillary pressure and peat structure on bubble storage using concepts from electromagnetism and hydrostatics. To explore this model, bubble accumulation in a peat block from a subtropical wetland was observed over 102 days. The results highlight a hotspot layer of bubble accumulation at depths between 5 and 10 cm below the monolith surface. Based on the corresponding power spectra of returned electromagnetic energy, bubbles in this shallow hotspot layer were larger relative to those in deeper layers, while the degree of decomposition of the upper layers was generally smaller than that of the lower layers based on von Post humification tests. X-ray CT from different depths revealed a barrier structure of low void ratio (r1) just above this hotspot. Our findings suggest that bubble capacitance of a peat layer is related to (1) the difference in size between gas bubbles and peat pores, and (2) the void ratio, both being a function of peat structure. This work has implications for better understanding how changes in water table elevation associated with climate change and sea level rise (particularly for freshwater wetlands near coastal areas like the U.S. Everglades) may potentially alter bubble sizes, and thus bubble storage in peat soils.

Acknowledgments
This material is partly based upon work supported by the National Science Foundation under grant EAR 1623895 and National Oceanic and Atmospheric Administration (NOAA) under grant GC11–337. We thank William Wright (Florida Atlantic University), and Greg Mount (currently at Indiana University of Pennsylvania) for assistance in collecting the peat sample. We thank Vassil Karloukovski (Lancaster University) for providing X-ray CT images and Neil Terry (United States Geological Survey) for valuable discussions regarding scattering phenomena. The first author acknowledges the support of the China Scholarship Council (CSC). Any additional data can be obtained from HydroShare (http://www.hydroshare.org/resource/762bbda0582744158d845afe0f6f27e0).

References

Baird, A. J., Beckwith, C. W., Waldron, S., & Waddington, J. M. (2004). Ebullition of methane-containing gas bubbles from near-surface Sphagnum peat. *Geophysical Research Letters*, *31*, L121505. https://doi.org/10.1029/2004GL021157

Baird, A. J., & Waldron, S. (2003). Shallow horizontal groundwater flow in peatlands is reduced by bacteriogenic gas production. *Geophysical Research Letters*, *30*(20). https://doi.org/10.1029/2003GL018233

Beckwith, C. W., & Baird, A. J. (2001). Effect of biogenic gas bubbles on water flow through poorly decomposed blanket peat. *Water Resources Research*, *37*(3), 551–558. https://doi.org/10.1029/2000WR900303

Berndt, C., Feseker, T., Treude, T., Krastel, S., Liebetrau, V., Niemann, H., et al. (2014). Temporal constraints on hydrate-controlled methane seepage off Svalbard. *Science*, *343*(6168), 284–287. https://doi.org/10.1126/science.1246298

Blais, K. E. (2005). *Measurement of physical and hydraulic properties of organic soil using computed tomographic imagery* (Master's thesis). Burnaby, Canada: Simon Fraser University.

Boudreau, B. P. (2012). The physics of bubbles in surficial, soft, cohesive sediments. *Marine Petroleum Geology*, *38*(1), 1–18. https://doi.org/10.1016/j.marpetgeo.2012.07.002

Cassidy, N. J. (2008). GPR attenuation and scattering in a mature hydrocarbon spill: A modeling study. *Vadose Zone Journal*, *7*(1), 140–159. https://doi.org/10.2136/vzj2006.0142

Chen, X., & Slater, L. (2015). Gas bubble transport and emissions for shallow peat from a northern peatland: The role of pressure changes and peat structure. *Water Resources Research*, *51*, 151–168. https://doi.org/10.1002/2014WR016268

Chen, X., V. R., Schäfer, K., & Slater, L. (2017). Methane emission through ebullition from an estuarine mudflat: 2. Field observations and modeling of occurrence probability. *WaterResourcesResearch*, https://doi.org/10.1002/2016WR019720

Ciais, P., Sabine, C., Bala, G., Bopp, L., Brovkin, V., Canadell, J., et al. (2013). Carbon and other biogeochemical cycles. In T. F. Stocker, et al. (Eds.), *Climate change 2013: The physical science basis. Contribution of working group I to the fifth assessment report of the intergovernmental panel on climate change* (pp. 465–570). Cambridge, UK: Cambridge University Press.

Clennell, M., Henry, P., Hovland, M., Booth, J. S., Winters, W. J., & Thomas, M. (2000). Formation of natural gas hydrates in marine sediments: Gas hydrate growth and stability conditioned by host sediment properties. *Annals New York Academy Sciences*, *912*(1), 887–896. https://doi.org/10.1111/j.1749-6632.2000.tb06842.x

Comas, X., & Slater, L. (2007). Evolution of biogenic gases in peat blocks inferred from noninvasive dielectric permittivity measurements. *Water Resources Research*, *43*, W05424. https://doi.org/10.1029/2006WR005562

Comas, X., Slater, L., & Reeve, A. (2005). Spatial variability in biogenic gas accumulations in peat soils is revealed by ground penetrating radar (GPR). *Geophysical Research Letters*, *32*, L08401. https://doi.org/10.1029/2004GL022297

Comas, X., Slater, L., & Reeve, A. (2007). In situ monitoring of free-phase gas accumulation and release in peatlands using ground penetrating radar (GPR). *Geophysical Research Letters*, *34*, L06402. https://doi.org/10.1029/2006GL029014

Comas, X., Slater, L., & Reeve, A. (2011). Atmospheric pressure drives changes in the vertical distribution of biogenic free-phase gas in a northern peatland. *Journal Geophysical Research*, *116*, G04014. https://doi.org/10.1029/2011JG001701

Corapcioglu, M. Y., Cihan, A., & Drazenovic, M. (2004). Rise velocity of an air bubble in porous media: Theoretical studies. *Water Resources Research*, *40*, W04214. https://doi.org/10.1029/2003WR002618

Coulthard, T., Baird, A., Ramirez, J., & Waddington, J. (2009). Methane dynamics in peat: Importance of shallow peats and a novel reduced-complexity approach for modeling ebullition. In A. J. Baird et al. (Eds.), *Carbon Cycling Northern Peatlands* (pp. 173–185). Washington, DC: American Geophysical Union. https://doi.org/10.1029/2008GM000811

Craft, C. B., & Richardson, C. J. (2008). Soil characteristics of the Everglades peatland. In C. J. Richardson (Ed.), *Everglades experiments* (pp. 59–72). New York, NY: Springer Science & Business Media.

DelSontro, T., McGinnis, D. F., Wehrli, B., & Ostrovsky, I. (2015). Size does matter: Importance of large bubbles and small-scale hot spots for methane transport. *Environmental Science & Technology*, *49*(3), 1268–1276. https://doi.org/10.1021/es5054286

Ebrahimi, A., & Or, D. (2017). Mechanistic modeling of microbial interactions at pore to profile scales resolve methane emission dynamics from permafrost soil. *Journal Geophysical Research: Biogeosciences*, *122*, 1216–1238. https://doi.org/10.1002/2016JG003674

Fechner-Levy, E. J., & Hemond, H. F. (1996). Trapped methane volume and potential effects on methane ebullition in a northern peatland. *Limnology Oceanography*, *41*(7), 1375–1383. https://doi.org/10.4319/lo.1996.41.7.1375

Frank, P. I., David, P. D., Theodore, L. B., & Lavine, A. S. (2006). *Fundamentals of heat and mass transfer* (6th Ed.). New York, NY: John Willey and Sons.

Glaser, P. H., Chanton, J. P., Morin, P., Rosenberry, D. O., Siegel, D. I., Ruud, O., et al. (2004). Surface deformations as indicators of deep ebullition fluxes in a large northern peatland. *Global Biogeochemical Cycles*, *18*, GB1003. https://doi.org/10.1029/2003GB002069

Granberg, G., Ottosson-Löfvenius, M., Grip, H., Sundh, I., & Nilsson, M. (2001). Effect of climatic variability from 1980 to 1997 on simulated methane emission from a boreal mixed mire in northern Sweden. *Global Biogeochemical Cycles*, *15*(4), 977–991. https://doi.org/10.1029/2000GB001356

Greinert, J., & Nützel, B. (2004). Hydroacoustic experiments to establish a method for the determination of methane bubble fluxes at cold seeps. *GeoMarine Letters*, *24*(2), 75–85. https://doi.org/10.1007/s00367-003-0165-7

Hamilton, S. (2007). *An analog electronics companion: Basic circuit design for engineers and scientists*. Cambridge, UK: Cambridge University Press.

Hutchison, C. E. (1957). *A treatise of limnology. Volume 1: Geography, physics and chemistry*. New York, NY: Wiley.

IPCC (2007). Climate change 2007: The physical science basis. In S. Solomon (Ed.), *Contribution of working group I to the fourth assessment report of the intergovernmental panel on climate change* (Vol. 4). Cambridge, UK: Cambridge University Press.

IPCC (2013). Climate change 2013: The physical science basis. In T. F. Stocker et al. (Eds.), *Contribution of working group I to the fifth assessment report of the intergovernmental panel on climate change*(p. 1533). Cambridge, UK: Cambridge University Press.

Jain, A. K., & Juanes, R. (2009). Preferential Mode of gas invasion in sediments: Grain-scale mechanistic model of coupled multiphase fluid flow and sediment mechanics. *Journal Geophysical Research*, *114*, B08101. https://doi.org/10.1029/2008JB006002

Jones, S., Evans, G., & Galvin, K. (1999). Bubble nucleation from gas cavities: A review. *Advances Colloid Interface Science*, *80*(1), 27–50. https://doi.org/10.1016/S0001-8686(98)00074-8

Kellner, E., & Lundin, L.-C. (2001). Calibration of time domain reflectometry for water content in peat soil. *Hydrology Research*, *32*(4–5), 315–332. https://doi.org/10.1029/WR026i010p02267

Kellner, E., Baird, A. J., Oosterwoud, M., Harrison, K., & Waddington, J. M. (2006). Effect of temperature and atmospheric pressure on methane (CH4) ebullition from near-surface peats. *Geophysical Research Letters*, *33*, L18405. https://doi.org/10.1029/2006GL027509

Kettridge, N., & Binley, A. (2008). X-ray computed tomography of peat soils: Measuring gas content and peat structure. *Hydrological Processes*, *22*(25), 4827–4837. https://doi.org/10.1002/hyp.7097

Kettridge, N., & Binley, A. (2011). Characterization of peat structure using X-ray computed tomography and its control on the ebullition of biogenic gas bubbles. *Journal Geophysical Research*, *116*, G01024. https://doi.org/10.1029/2010JG001478

Kirby, B. J. (2010). *Micro-and nanoscale fluid mechanics: Transport in microfluidic devices*. Cambridge, UK: Cambridge University Press.

Li, X., & Yortsos, Y. (1995a). Theory of multiple bubble growth in porous media by solute diffusion. *Chemical Engineering Science*, *50*(8), 1247–1271. https://doi.org/10.1016/0009-2509(95)98839-7

Li, X., & Yortsos, Y. (1995b). Visualization and simulation of bubble growth in pore networks. *AIChE Journal*, *41*(2), 214–222. https://doi.org/10.1002/aic.690410203

Liu, L., Wilkinson, J., Koca, K., Buchmann, C., & Lorke, A. (2016). The role of sediment structure in gas bubble storage and release. *Journal Geophysical Research: Biogeosciences*, *121*, 1992–2005. https://doi.org/10.1002/2016JG003456

Marfunin, A. S. (1994). *Advanced mineralogy: composition, structure, and properties of mineral matter: Concepts, results, and problems* (Vol. 1). Berlin/Heidelberg, DE: Springer-Verlag.

Martens, C. S., & Albert, D. B. (1994). Biogeochemical processes controlling gas production, consumption, and transport in organic-rich marine sediments. In T. F. Wever (Ed.), *Proceedings of the Gassy Mud Workshop* (pp. 101–107). Kiel, Germany: FWG.

Mustasaar, M., & Comas, X. (2017). Spatiotemporal variability in biogenic gas dynamics in a subtropical peat soil at the laboratory scale is revealed using high-resolution ground-penetrating radar. *Journal Geophysical Research: Biogeosciences*, *122*, 2219–2232. https://doi.org/10.1002/2016JG003714

Parsekian, A. D., Slater, L., & Giménez, D. (2012). Application of ground-penetrating radar to measure near-saturation soil water content in peat soils. *Water Resources Research*, *48*, W02533. https://doi.org/10.1029/2011WR011303

Quinton, W. L., Elliot, T., Price, J. S., Rezanezhad, F., & Heck, R. (2009). Measuring physical and hydraulic properties of peat from X-ray tomography. *Geoderma*, *153*(1), 269–277. https://doi.org/10.1016/j.geoderma.2009.08.010

Quinton, W. L., Gray, D. M., & Marsh, P. (2000). Subsurface drainage from hummock-covered hillslopes in the Arctic tundra. *Journal Hydrology*, *237*(1), 113–125. https://doi.org/10.1016/S0022-1694(00)00304-8

Quinton, W. L., Hayashi, M., & Carey, S. K. (2008). Peat hydraulic conductivity in cold regions and its relation to pore size and geometry. *Hydrological Processes*, *22*(15), 2829–2837. https://doi.org/10.1002/hyp.7027

Ramirez, J. A., Baird, A. J., & Coulthard, T. J. (2016). The effect of pore structure on ebullition from peat. *Journal Geophysical Research: Biogeosciences*, *121*, 1646–1656. https://doi.org/10.1002/2015JG003289

Ramirez, J. A., Baird, A. J., Coulthard, T. J., & Waddington, J. M. (2015). Testing a simple model of gas bubble dynamics in porous media. *Water Resources Research*, *51*, 1036–1049. https://doi.org/10.1002/2014WR015898

Rezanezhad, F., Quinton, W. L., Price, J. S., Elrick, D., Elliot, T. R., & Heck, R. J. (2009). Examining the effect of pore size distribution and shape on flow through unsaturated peat using computer tomography. *Hydrology Earth System Sciences*, *13*, 1993–2002. https://doi.org/10.5194/hess-13-1993-2009

Richards, L. A. (1931). Capillary conduction of liquids through porous mediums. *Physics*, *1*(5), 318–333. https://doi.org/10.1063/1.1745010

Rosenberry, D. O., Glaser, P. H., & Siegel, D. I. (2006). The hydrology of northern peatlands as affected by biogenic gas: Current developments and research needs. *Hydrological Processes*, *20*(17), 3601–3610. https://doi.org/10.1002/hyp.6377

Rosenberry, D. O., Glaser, P. H., Siegel, D. I., & Weeks, E. P. (2003). Use of hydraulic head to estimate volumetric gas content and ebullition flux in northern peatlands. *Water Resources Research*, *39*(3), 1066. https://doi.org/10.1029/2002WR001377

Rothfuss, F., & Conrad, R. (1994). Development of a gas diffusion probe for the determination of methane concentrations and diffusion characteristics in flooded paddy soil. *FEMS Microbiology Ecology*, *14*(4), 307–318.

Shannon, R. D., White, J. R., Lawson, J. E., & Gilmour, B. S. (1996). Methane efflux from emergent vegetation in peatlands. *Journal Ecology*, *84*, 239–246. https://doi.org/10.2307/2261359

Strack, M., Kellner, E., & Waddington, J. (2005). Dynamics of biogenic gas bubbles in peat and their effects on peatland biogeochemistry. *Global Biogeochemical Cycles*, *19*, GB1003. https://doi.org/10.1029/2004GB002330

Terry, N., & Slater, L. (2017). Gas bubble size estimation in peat soils from EM wave scattering observed with ground penetrating radar. *Water Resources Research*, *53*, 2755–2769. https://doi.org/10.1002/2016WR019783

Tokida, T., Miyazaki, T., & Mizoguchi, M. (2005). Ebullition of methane from peat with falling atmospheric pressure. *Geophysical Research Letters*, *32*, L13823. https://doi.org/10.1029/2005GL022949

Topp, G. C., Davis, J., & Annan, A. P. (1980). Electromagnetic determination of soil water content: Measurements in coaxial transmission lines. *Water Resources Research*, *16*(3), 574–582. https://doi.org/10.1029/WR016i003p00574

von Post, L. (1922). Swedish geological peat survey with the results obtained so far (in Swedish). *Svenska Mosskulturföreningens Tidskrift*, *36*, 1–27.

Walter, B. P., & Heimann, M. (2000). A process-based, climate-sensitive model to derive methane emissions from natural wetlands: Application to five wetland sites, sensitivity to model parameters, and climate. *Global Biogeochemical Cycles*, *14*(3), 745–765. https://doi.org/10.1029/1999GB001204

Walter, B. P., Heimann, M., Shannon, R. D., & White, J. R. (1996). A process-based model to derive methane emissions from natural wetlands. *Geophysical Research Letters*, *23*(25), 3731–3734. https://doi.org/10.1029/96GL03577

Wright, W., & Comas, X. (2016). Estimating methane gas production in peat soils of the Florida Everglades using hydrogeophysical methods. *Journal Geophysical Research: Biogeosciences*, *121*, 1190–1202. https://doi.org/10.1002/2015JG003246

Yortsos, Y. C., & Parlar, M. (1989). Phase change in binary systems in porous media: Application to solution-gas drive. Paper presented at 64th annual technical conference and exhibition, Society of Petroleum Engineers, San Antonio, TX. https://doi.org/doi.org/10.2118/19697-MS

Yousfi, E., Zarcone, C., Bories, S., & Lenormand, R. (1990). *Liberation of solution gas during pressure depletion in a 2-dimensional porous medium*. Paper presented at IFP Research Conference, Arles, France.

Yu, C., Warrick, A., & Conklin, M. (1999). Derived functions of time domain reflectometry for soil moisture measurement. *Water Resources Research*, *35*(6), 1789–1796. https://doi.org/10.1029/1999WR900025